Examination of the influence of La promotion on Ni state in hydrotalcite-derived catalysts under CO2 methanation reaction conditions: Operando X-ray absorption and emission spectroscopy investigation

Dominik Wierzbicki, Rafal Baran, Radoslaw Dębek, Monika Motak, Maria Elena Gálvez, Teresa Grzybek, Patrick da Costa, Pieter Glatzel

Examination of the influence of La promotion on Ni state in hydrotalcite-derived catalysts under CO_2 methanation reaction conditions: Operando X-ray absorption and emission spectroscopy investigation

Dominik Wierzbicki[a,b,*], Rafal Baran[c,*], Radosław Dębek[a], Monika Motak[a], Maria Elena Gálvez[b], Teresa Grzybek[a], Patrick Da Costa[b], Pieter Glatzel[c]

[a]AGH University of Science and Technology, Faculty of Energy and Fuels, Al. A. Mickiewicza 30, 30-059 Cracow, Poland

[b]Sorbonne Université, Institut Jean Le Rond d'Alembert, CNRS UMR 7190, 2 place de la gare de ceinture, 78210 Saint-Cyr-L'Ecole, France

[c]ESRF – European Synchrotron Radiation Facility, 71 Avenue des Martyrs, Grenoble, France

**Corresponding author:* dwierzb@agh.edu.pl; rafal.baran@esrf.fr

Keywords: CO_2, Methanation, Nickel, Lanthanum, XAS, XES

Abstract

Hydrotalcite-derived Ni-containing and Ni-La promoted catalysts showed very high activity in CO_2 methanation, which is an efficient way of carbon dioxide conversion into methane – a valuable product. The catalysts were obtained by co-precipitation method followed by thermal decomposition and characterized by elemental analysis, low temperature nitrogen sorption, XRD, H_2-TPR, CO_2-TPD and TEM. The obtained results confirmed the formation of periclase-like structure materials, with nickel present as NiO nanoparticles and suggested successful incorporation of lanthanum into the catalytic system. The addition of lanthanum changed the interaction between nickel and periclase matrix (H_2-TPR) and changed the distribution of basic sites, especially medium strength ones (CO_2-TPD). Moreover, the catalysts were studied by complementary HERFD-XANES and XES spectroscopy under model operando conditions. The results uncovered that the presence of lanthanum strongly influenced the chemical nature and oxidation state of nickel species and its crucial role in catalyst activity enhancement in CO_2 methanation reaction.

1. Introduction

The energy transition to renewable sources, as well as growing concentration of carbon dioxide in the atmosphere, which is considered to be the major drive of climate change and greenhouse effect, led to an increased interest in the reaction of CO_2 hydrogenation. In order to overcome the gap between electricity production and immediate demand it is crucial to develop suitable storage systems. Hydrogenation of carbon dioxide offers the possibility of storing excess energy in the form of chemicals such as methane or higher hydrocarbons, with hydrogen provided via water electrolysis using excess energy. The existing infrastructure for gas transportation enables to use methane as an energy carrier [1]. Hydrogenation of CO_2 (methanation and Fischer-Tropsch synthesis) is treating carbon dioxide as a feedstock and may lead simultaneously to the production of liquid and/or gaseous fuels, CO_2 emissions reduction and/or storage of excess energy in the form of chemicals.

Carbon dioxide methanation reaction was mostly carried out using catalysts based on 8-10 group metals (Ni, Pt, Ir, Fe, Ru, Co, Rh) [2-7] of which nickel, ruthenium and rhodium based catalysts have been found to be the most active in this process [7, 8]. Nickel-based catalysts are the most extensively studied because Ni shows very good activity in the reaction of CO_2 hydrogenation and is much cheaper and more abundant than precious metals, which from the commercial standpoint makes it more interesting. However, the catalytic activity at lower temperatures still needs to be enhanced. This fact motivated the development of novel Ni-based catalysts highly active at low reaction temperatures. Hydrotalcites (layered double hydroxides - LDHs) were chosen as catalyst precursors. LDHs are mixed hydroxides of di- and trivalent metals, present in brucite-like layers ($Mg(OH)_2$) with anions present in the interlayer spaces compensating the positive charge. Lately, we have shown that divalent Ni^{2+}, as well as,

trivalent La^{3+} may be also incorporated into LDHs structure without formation of any additional phase [9]. As a result, the acid-base sites and redox properties can be perfectly tailored for catalytic application e.g. CO_2 methanation [9-11]. The cations present in brucite-like layers are randomly distributed, which leads to high homogeneity of the synthesized materials. Additionally, the composition of such material can be easily controlled during the synthesis. Therefore hydrotalcite-derived materials can be adjusted for the reaction of CO_2 methanation, in order to fulfil the requirements such as high basicity (CO_2 adsorption capacity), appropriate nickel distribution and reducibility (redox properties).

Up to now only few publications have been devoted to hydrotalcite-derived catalysts for CO_2 methanation [10-12]. In our previous studies we found that increasing the Ni content in hydrotalcites resulted in different medium-strength basic sites distribution, which increased with increasing nickel content and resulted in better performance in CO_2 methanation reaction [13]. It was also found that the incorporation of La increased the amount of medium-strength basic sites and weakened the interaction between Ni and the support (increased reducibility), which resulted in much better performance of such catalysts in methanation of CO_2 [14]. The promoting effect was strongly dependent on the method of lanthanum incorporation [9]. Despite new findings the reaction pathway and the role of promoters remain an open question. Recently, both theoretical (DFT calculation) and experimental (FTIR, XAFS) approaches have been used to describe surface chemical activity of Ni-containing catalyst in methanation process [15-18]. The mechanisms proposed in literature are an associative [19] and dissociative mechanism [20]. The former proposes the formation of oxygenate intermediates, subsequently hydrogenated to CH_4 while the latter assumes dissociation of CO_2 to adsorbed CO and O, with subsequent hydrogenation to CH_4. However, in general it is accepted that CO is the main

intermediate in CO_2 methanation. It was established before that synchrotron-based techniques are excellent tools to study the local coordination of active species and behaviour of catalysts under realistic conditions [21, 22]. Using element specific X-ray photon-in/photon-out techniques such as high energy resolution fluorescence detected X-ray absorption (HERFD-XANES) and X-ray emission spectroscopies (XES) it is possible to identify adsorbed species on catalyst sites, probe the chemical information from ligand and calculate bond distances.

The goal of this work was to study the properties of nickel-containing lanthanum-promoted hydrotalcite-derived mixed oxides with constant M^{II+}/M^{III+} ratio. In order to elucidate the role of lanthanum in CO_2 methanation, operando HERFD-XANES and XES were implemented to study the local coordination and oxidation state of nickel in hydrotalcite-derived catalysts during reduction and methanation of carbon dioxide reaction. We believe that valence-to-core-XES spectroscopy was used for the first time to study ligand environment of Ni species under realistic condition in this process.

2. Experimental

2.1. Synthesis of the materials

Hydrotalcite-like materials containing di- and trivalent metals (Ni, Mg, Al and La), were obtained using co-precipitation method at constant pH (9.5-10). Two aqueous solutions: (i) containing nitrates of divalent and trivalent metals and (ii) 1 M sodium hydroxide were added dropwise into a flask containing an aqueous solution of sodium carbonate (65°C) under constant controlled pH (9.5-10) and vigorous stirring. The mixture was aged for 1h at 65°C, filtered, washed with distilled water and dried at 80°C overnight. The obtained hydrotalcite materials were calcined at 500°C for 5h, and then some amount of each of them was reduced

at 800ºC in stream of 5% H_2/Ar. The sample nomenclature depending of undergone treatment is collated in Table 1. The concentration of the nickel, magnesium, alumina and lanthanum, determined by XRF, is listed in Table 2.

Table 1. Sample labelling according to corresponding treatment

Sample label	as-synthesised	calcined	reduced	operando conditions at 300 ºC		
				H_2	CO_2	CO_2 + H_2
Ni40	+					
Ni40La2	+					
Ni40_calc	+	+				
Ni40La2_calc	+	+				
Ni40_red	+	+	+			
Ni40La2_red	+	+	+			
Ni40_ H_2	+	+	+	+		
Ni40La2_ H_2	+	+	+	+		
Ni40_ CO_2	+	+	+		+	
Ni40La2_ CO_2	+	+	+		+	
Ni40_ CO_2+H_2	+	+	+			+
Ni40La2_CO_2+H_2	+	+	+			+

2.2. Physico-chemical characterization

The obtained hydrotalcite-derived catalysts were characterized by low temperature nitrogen sorption, X-ray fluorescence spectroscopy (XRF), X-ray diffraction (XRD), high energy resolution fluorescence detected X-ray absorption near edge structure spectroscopy (HERFD-XANES), X-ray emission spectroscopy (XES), transmission electron microscopy

(TEM), hydrogen temperature-programed reduction (H_2-TPR) and carbon dioxide temperature-programed desorption (CO_2-TPD).

X-ray diffraction measurements were carried out on PANalytical-Empyrean diffractometer equipped with CuK_α radiation source (λ = 1.5406Å) within 2θ range from 3 to 90°, with a 0.02°/min step size. Crystallite sizes were calculated using the Scherrer equation. The textural properties of reduced samples - specific surface area and total pore volume - were determined from nitrogen adsorption isotherms (-196°C), obtained using a Belsorp Mini II apparatus (BEL Japan). Prior to the measurements the samples were outgassed at 110°C under vacuum for 3h.

The HERFD-XANES and XES experiments were carried out at ID26 beamline of the European Synchrotron Radiation Facility (ESRF) in Grenoble, France equipped with three undulators providing a flux of 10^{13} photons s^{-1}. The beam size on the sample was 1 (horizontal) x 0.1 (vertical) mm^2. The incident energy was tuned through the Ni K edge by a cryogenically cooled Si(111) double-crystal monochromator. A Ni foil was used to calibrate energy by setting the first inflection point of the Ni K edge at 8333 eV. The emission spectrometer was equipped with five Si(551) crystal analysers in Roland circle geometry. High-Energy Resolution Fluorescence Detected X-ray Absorption Near Edge Structure (HERFD-XANES) spectra were recorded by scanning the incident energy and detecting the fluorescence at the maximum of $K\beta_{1,3}$ emission line. X-ray emission spectra in core-to-core (CTC) and valence-to-core (VTC) ranges were recorded at 8500 eV excitation energy. The XES and XANES spectra were normalized with respect to the area. The spectra were not corrected for self-absorption effects. The conclusions drawn in the context of the present study are not affected by such spectral

distortions. The background subtraction was carried out for the Ni VTC-XES spectra in order to remove the contribution of the CTC main line tail by applying the procedure proposed by Gallo and Glatzel [23]. The data of reference samples NiO and $Ni(OH)_2$ was recorded on the pellets containing 5 wt. % of the sample diluted with cellulose. The spectrum of metallic nickel was obtained from Ni foil (4 μm).

Sieved fractions of Ni40_calc and Ni40La2_calc catalysts (100 – 200 μm) were pressed at ~2 ton cm^{-2} into 0.5 mm thin wafers of ca. 75 mg cm^{-2} and placed inside Maxthal® cell. The Maxthal® is an heating cell developed at Sample Environment unit of ESRF and it is in a pool of shared equipment, making it freely accessible to all ESRF users [24, 25]. More information and characteristic about furnace is included in Supporting Information document. This in-situ cell integrated in a devoted gas-flow setup was used as a reactor in operando experiments. The cell was positioned at the focus of the spectrometer at 45° with respect to the incident beam and silicon analysers. The desired concentrations of H_2 (60 vol. %) and CO_2 (15 vol. %) were obtained by mixing pure gases with He as inert carrier. The gas flow was kept at 35 cm^3 min^{-1}. The CO_2 conversion and CH_4 yield was monitored by μGC analyser equipped with MS5A (10 m) and PPU (8 m) columns and TCD detector. Before reaction the catalysts were reduced in-situ in the flow of 12.5 % H_2/He at 750 ^oC. The data analysis for HERFD-XANES was conducted with Athena software of IFEFFIT package.

Temperature-programmed reduction (H_2-TPR) profiles were obtained using BELCAT-M equipped with a TCD detector. The calcined materials (50 mg for each experiment) were first outgassed at 100°C for 2h and then reduced using 5%H_2/Ar at a heating rate of 7.5°Cmin^{-1} from 100°C to 900°C. Temperature-programmed desorption (CO_2-TPD) was performed on the

same device (BELCAT-M) for the reduced samples. The materials were degassed for 2h in a stream of He at 500°C and cooled to 80°C. After outgassing, a mixture of 10%CO_2/He was fed for 1h in order to adsorb CO_2. Afterwards a flow of He was introduced for 15 minutes in order to desorb weakly adsorbed CO_2. Then the material was heated (10°C /min) under He flow from 80°C to 900°C in order to determine the evolution of CO_2. The concentration of desorbed CO_2 was measured with a TCD detector.

The catalysts before and after the methanation reaction were examined by Transmission Electron Microscopy (TEM, JOEL JEM-100XCII, acceleration voltage of 100keV). Based on the analysis of the obtained images, the distribution of nickel particle size was discussed. The determination of particle size distribution involved the analysis of at least 300 Ni particles. The measurements of Ni particle size were performed with the aid of ImageJ software. Based on the results obtained from TEM the Ni dispersion was calculated using the method proposed in Chapter 3.1.2 of 'Handbook of heterogenous catalysis' by G.Bergeret and P.Gallezot [26].

2.3. Catalytic measurements

The performance of the catalysts in CO_2 methanation reaction was evaluated in a tubular quartz reactor at atmospheric pressure, with a K-type thermocouple inside catalyst bed. Prior to the reaction the catalysts were reduced in-situ under a 100 ml/min flow of 10%H_2/He at 900°C with the temperature ramp of 10°C/min for 1h. The feed gas 15 vol. % CO_2/60 vol. % H_2/25 vol. %Ar = 3/12/5 was then fed into the system with GHSV = 12000 h^{-1}. The gas products including CO, CH_4, H_2 and CO_2 were analysed using an online micro-chromatograph (Varian 4900). The CO_2 methanation catalytic tests were performed from 250°C to 450°C with steady-state operation for 30 minutes (every 50°C). The activation energies were calculated using

power rate law [20]. The TOF value was calculated supposing that all the exposed Ni atoms participate in the reaction. The amount of surface Ni was calculated based on the analysis of TEM results (Ni dispersion).

$$TOF = \frac{nCH_4(mol)}{nNi\ (mol) * t(s)}$$

3. Results and discussion

3.1. Structural and textual properties

Table 1 contains the results of low temperature nitrogen sorption and elemental analysis for the reduced samples. The content of Ni and La measured with XRF are close to calculated before synthesis. The typical textural properties, specific surface area (S_{BET}) and total pore volume (V_{tot}), of synthetic hydrotalcite-derived materials are in the ranges of 100-180 $m^2\ g^{-1}$ and 0.3 – 0.7 $cm^3\ g^{-1}$, respectively. Due to high Ni loading the values of S_{BET} and V_{tot} of reduced Ni40 and Ni40La2 are a bit below this range. This result stays in good agreement with previous study of Dębek et al. [27]. Furthermore, from Table 2 it may be observed that the incorporation of 2.6 wt. % of lanthanum did not significantly influenced textural properties of the catalyst.

Table 2 Specific surface area S_{BET}, total pore volume V_{tot} and elemental analysis results for the Ni and Ni/La hydrotalcite-derived catalysts

Catalyst	textural properties		chemical analysis					
	Specific surface area (S_{BET}) [m^2/g][a]	Total pore volume (V_{tot}) [cm^3/g]			Ni [%]	Mg [%]	La [%]	Al [%]
Ni40	71	0.27	fresh	wt.	40	1.9	-	6.8

				mol	0.67	0.08	-	0.25
			reduced	wt.	52.1	2.5	-	8.6
Ni40La2	72	0.25	fresh	wt.	40	1.5	2	6.3
				mol	0.68	0.067	0.015	0.235
			reduced	wt.	51.6	1.8	2.6	7.7

[a]The accuracy of S_{BET} determination is usually assumed to be ca. ± 5 %

Figure 1 shows the XRD diffractograms obtained for fresh, calcined, reduced and spent Ni40 and Ni40La2 samples. The patterns obtained for fresh hydrotalcites show reflections of 2θ at 11°, 24° and 35°, corresponding to (003), (006) and (009) planes, respectively indicating the existence of a layered hydrotalcite structure [28, 29]. The *a* and *c* unit cell parameter values were calculated basing on the methodology proposed by Rives et al [30]. Parameter c, which represents three times the distance between hydrotalcites layers, was calculated from the positions of the three first sharp reflections at 2θ between 10° and 40° ($c = d_{(003)} + 2d_{(006)} + 3d_{(009)}$). The value of c parameter is strongly dependent on the type of interlayer anions present in the hydrotalcites. As presented by Cavani et al. [31], this parameter allows defining the type of anions present in the interlayer. In case of our samples the *c* parameter values were in the range of 23.04 – 23.5Å, confirming the presence of carbonate and/or nitrate anions in the interlayer spaces. Parameter *a* value, which represents the average distance between the cations in the brucite-like layers, was ca. 3.04 Å for both samples. Since no other separate phase was observed, the obtained XRD results for fresh samples suggest successful incorporation of nickel into the hydrotalcite structure. The XRD patterns of the samples after calcination at 500°C are shown in Figure 1B. Typical reflections for periclase-like structure are observed at

2θ = 43.5° and 63°, as expected after thermal decomposition of hydrotalcites-like materials. No other phases were observed on the XRD diffractograms.

Figure 1C depicts the XRD patterns of the reduced hydrotalcite-derived mixed oxides. The diffractograms reveal the existence of periclase-like structure (MgO) and metallic nickel (Ni^0) phase. The latter with crystallite sizes ranging from 8-9 nm (calculated using Scherrer equation). No additional reflections arising from separate La phase/s were registered for Ni40La2 sample.

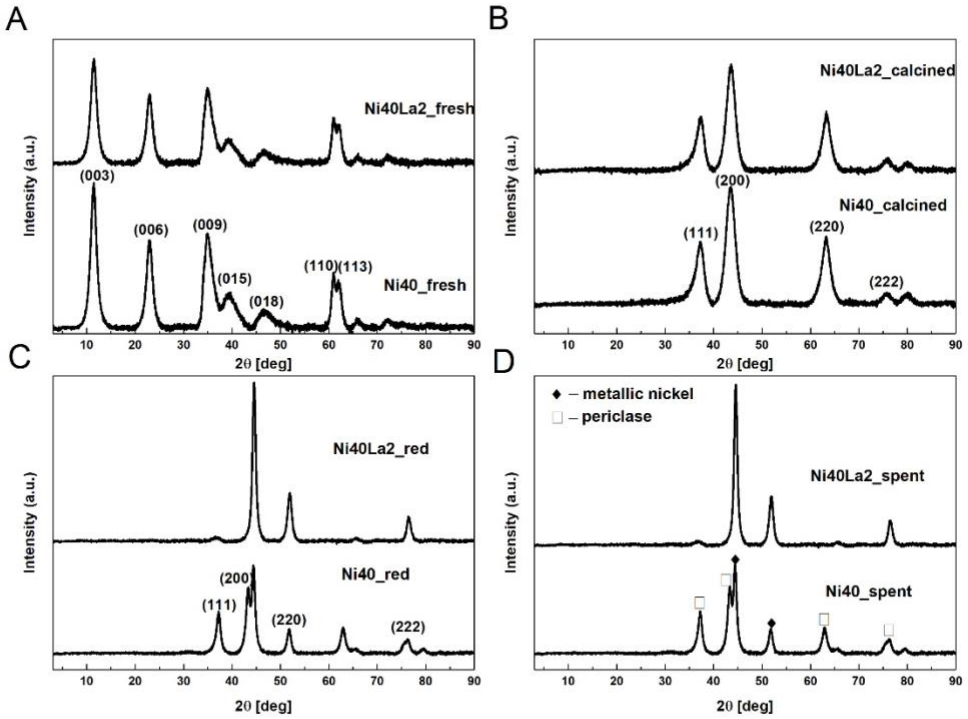

Figure 1 XRD patterns of a) as-synthesized b) calcined c) reduced d) spent (after catalytic tests) catalysts

3.2. Active sites and basicity

Figure 2 shows the H_2-TPR profiles obtained for the calcined catalysts. All profiles exhibit one asymmetric peak at temperature between 676-686°C, arising from the reduction of nickel

oxide species to metallic nickel (Ni^0). The reduction peak was registered at temperatures much higher than expected for the bulk nickel oxide or materials impregnated with nickel, and thus it may be assigned to nickel oxide in strong interaction with its surroundings [32]. This suggests the formation of a thermally stable solid phase of mixed oxides Mg(Ni,Al)O. The obtained H_2-TPR profiles show strong interaction between Ni and the support matrix, which suggests high dispersion degree of nickel. After the incorporation of lanthanum into the nickel containing hydrotalcite a small shift of the reduction peak to lower temperatures may be observed, from 686°C to 676°C for Ni40 and Ni40La2, respectively, indicating that La species facilitate the Ni(II) reduction. The obtained results suggest increased reducibility of nickel species, similarly as observed in our previous work [14].

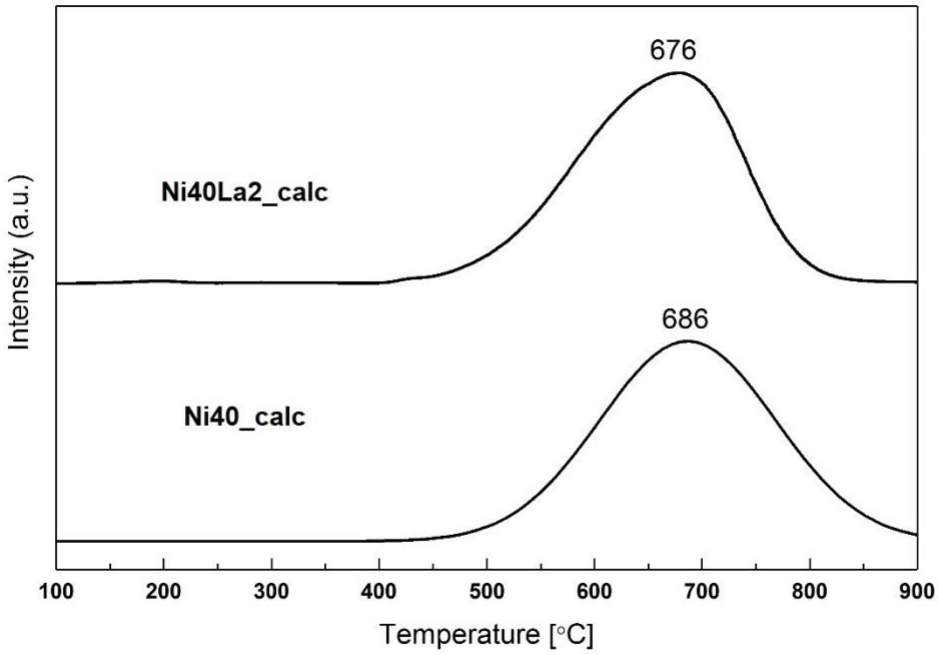

Figure 2 H_2-TPR profiles of the calcined materials

Figure 3 shows the CO_2-TPD profiles obtained for the hydrotalcite-derived mixed oxides after reduction at 900°C. The numbers of basic sites, calculated by integration of desorption peaks, which were deconvoluted into three Gaussian peaks corresponding to weak, medium strength and strong basic sites related to surface OH^-, acid-base Lewis pairs and low coordination surface O^{2-}, respectively [33], are presented in Table 3. The total basicity increased with La addition from 130 μmol/g to 211 μmol/g. This is in good agreement with our previous work where it was reported that the incorporation of La into Ni containing hydrotalcites increased the amount of medium strength basic sites. The incorporation of lanthanum into the nickel containing hydrotalcite influenced strongly the distribution of basic sites. There was observed: (i) a slight decrease of the amount of weak basic sites (ii) a

considerable increase in the amount of medium-strength sites and (iii) a slight increase in the amount of strong basic sites, when compared to Ni40.

Table 3 Basicity (CO_2-TPD) and crystallite sizes of Ni^0 particles (XRD), TOF, Ni dispersion and activation energy

Catalyst	Total basicity [μmol/g][a]	Weak basic sites [μmol/g][a]	Medium strength basic sites [μmol/g][a]	Strong basic sites [μmol/g][a]	Crystallite size [nm][b]		Ni dispersion [%][c]	TOF [10^{-2} s^{-1}][d]
					Reduced	Spent		
Ni40_red	130	32	59	39	8	7.6 / 9.1	7.6 / 9.1	3.1 / 6.2
Ni40La2_red	211	55	97	49	9	8.0 / 7.5	8.0 / 7.5	3.4 / 7.5

[a] The residual error of the measurement is in the range of 10 μmol/g
[b] The weighted residual error is in the range of 3-6% for the crystallite size
[c] The Ni dispersion was calculated based on the crystallite sizes obtained from TEM analysis (reduced / spent)
[d] GHSV= 12000 / 36000 h^{-1} and 250ºC

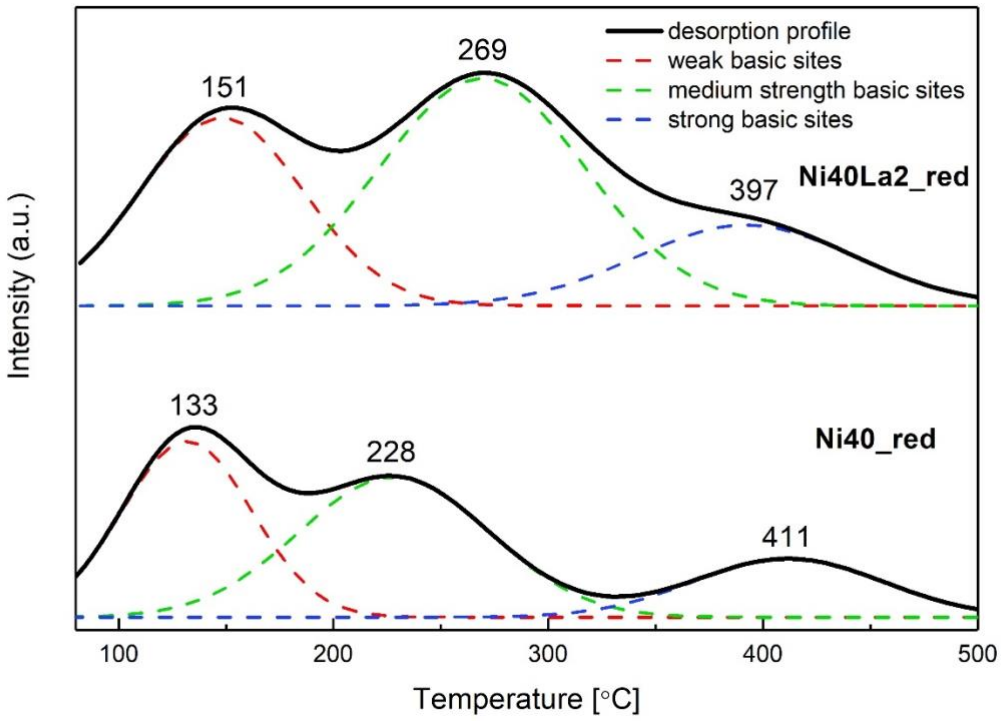

Figure 3 CO_2-TPD profiles of the reduced materials

3.3. Catalytic activity

The measurements of carbon dioxide conversion during catalytic methanation experiments are plotted in Figure 4, for both catalysts as a function of reaction temperature, and additionally for different gas hourly space velocity (12,000, 24,000 and 36,000 h^{-1}). The thick red continuous line represents the forecasted carbon dioxide conversion at thermodynamic equilibrium for the reaction carried out at conditions used in this work. The thermodynamics predicts almost complete CO_2 conversion at lower temperatures, which decreases with the increasing temperature, as a consequence of parallel reactions, e.g. reforming reactions resulting in the formation of undesired side-products, such as CO [34]. Both catalysts were

active in the reaction of CO_2 methanation. At GHSV = 12000 h^{-1} at 250°C the conversion reached 84.3 and 88.2 % for Ni40_red and Ni40La2_red, respectively i.e. almost thermodynamic equilibrium. Increasing the temperature to 350, 450 and 450°C resulted in quite similar CO_2 conversion, reaching thermodynamic equilibrium for both catalysts. As example at 300°C, CO_2 conversion decreased from 87.9% to 71.9 and 65.3% at GHSV of 12,000, 24,000 and 36,000 h^{-1}, respectively for Ni40 catalyst while for Ni40La2 the respective conversions were 91.8% to 77.6 and 69.3% for the same GHSV. The TOF values (Table 3) were 3.1 x 10^{-2} and 3.4 x 10^{-2} for Ni40 and Ni40La2, respectively at GHSV = 12000 h^{-1}. The calculated activation energies were 1.35 kJ/mol and 1.6 kJ/mol for Ni40La2 and Ni40, respectively. The values obtained are very low, in good agreement with the trend observed in Figure 4.

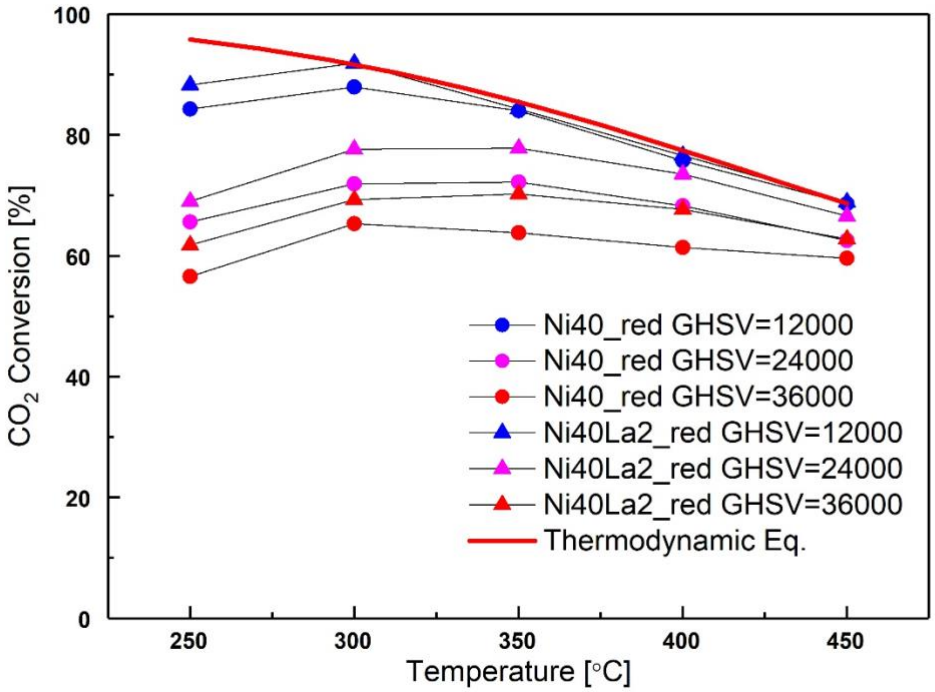

Figure 4 CO_2 conversion versus temperature at GHSV = 12000, 24000 and 36000h^{-1} for the studied catalysts

The introduction of La significantly increased catalyst activity due to two main factors. First one, lanthanum species are responsible for an increase in the population of medium strength basic sites by nearly twice compare to non-promoted catalyst. According to previous work of Pan et al. [29] the presence of medium strength centres favours formation of monodentate species, which are believed to be an intermediate in methane synthesis. It was found that, in comparison to bidentate species, monodentate species can be more easily hydrogenated. Secondly, as we state in the following chapters the presence of La strongly modifies the electronic structure of Ni leading to vast CO_2 adsorption on surface of Ni(0) nanoparticles with simultaneous change of Ni oxidation state, resulting in higher overall

activity. Thus, La plays a bi-functional role as a provider of medium strength basic sites as well as a modifier of Ni properties for CO_2 adsorption.Table S4 in SI document contains selected literature reports for nickel catalysts supported on different materials e.g. hydrotalcites, MgO, La_2O_3 or ZSM-5 together with the reaction conditions shedding light on various catalyst performance in the methanation process.

The selectivity towards methane as a function of temperature is plotted in Figure 5. Almost complete conversion towards methane, 99.0 and 99.6% for Ni40 and Ni40La2, respectively, was recorded for both catalysts at 250°C. As predicted by thermodynamic calculations, the selectivity towards methane decreased with increasing temperature, but only trace amounts of a side product carbon monoxide were recorded. Apart from CH_4 and CO, no other products were registered.

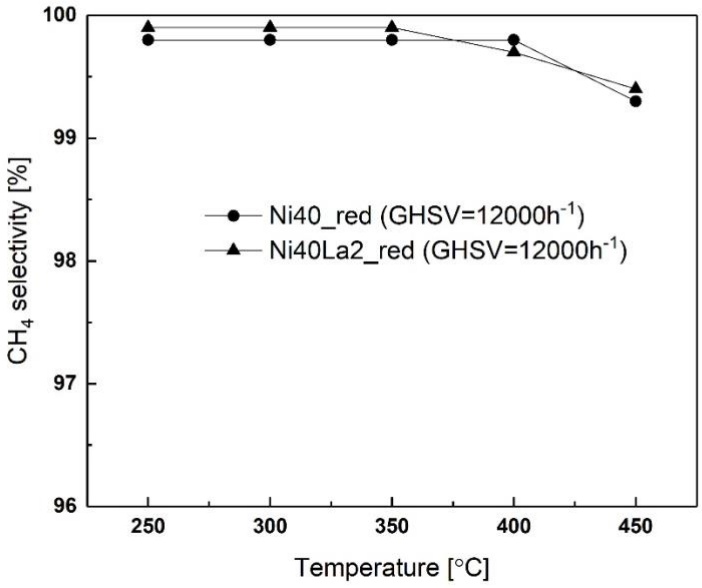

Figure 5 CH_4 selectivity versus temperature for obtained catalysts

In order to assess the stability of the studied catalysts, 24h-tests were performed at 250°C at GHSV = 12000h^{-1}(Fig 6). Almost no changes in activity were registered during stability tests.

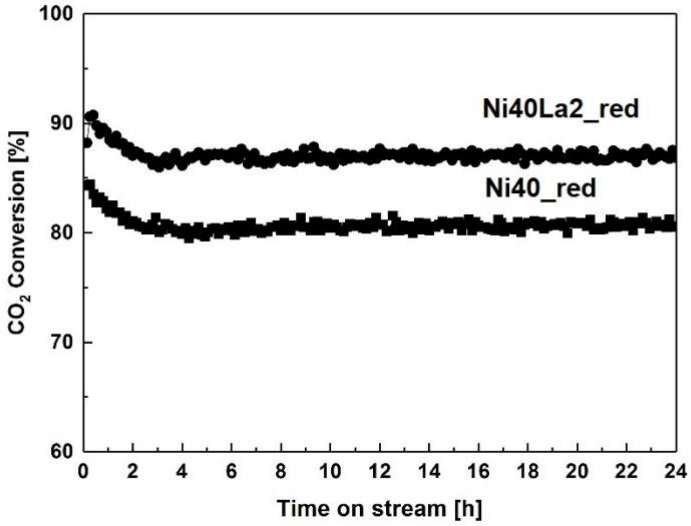

Figure 6 24h stability tests performed at 250℃ GHSV = 12000h^{-1}

3.4. Characterization of spent catalysts

Ni40 and Ni40La2 samples were characterized via XRD (Fig. 1D) and TEM (Fig. 7) after temperature-programmed methanation tests carried out with GHSV=12000h^{-1}. In order to examine structural and morphological changes in the catalysts the obtained results were compared to the ones registered for reduced samples.

XRD analysis showed that no changes of crystallite size were found for the spent (Fig. 1D) catalysts in comparison to reduced ones (Fig. 1D). Additionally no reflections arising from graphite phase were observed for diffractograms of spent catalysts, thus formation of graphite due to coking may be excluded, which is in good agreement with Garbarino et al. [35] and Abate et al. [11] who confirmed the absence of carbon depositions on Ni-Al-HT catalysts in CO_2 methanation. This stays in line with the results of TEM analysis (Fig. 7 B and D) as no carbon was observed in the TEM images recorded for spent samples.

The mean size of Ni particle size measured via TEM were in the same range as the values obtained from XRD (Table 2). Interestingly, Ni40_red sample exhibited larger Ni crystallite size than the spent catalysts, pointing to reorganisation of Ni crystallites upon methanation reaction. On the other hand, La promoted catalysts exhibited a small increase in Ni particle size upon methanation reaction indicating sintering of Ni species. As confirmed by H_2-TPR, La addition increased the reducibility of Ni species via decreasing interactions between nickel species in periclase hydrotalcite-derived structure and Mg(Ni,Al)O mixed oxides, which may explain small sintering of Ni crystallites observed for La promoted sample.

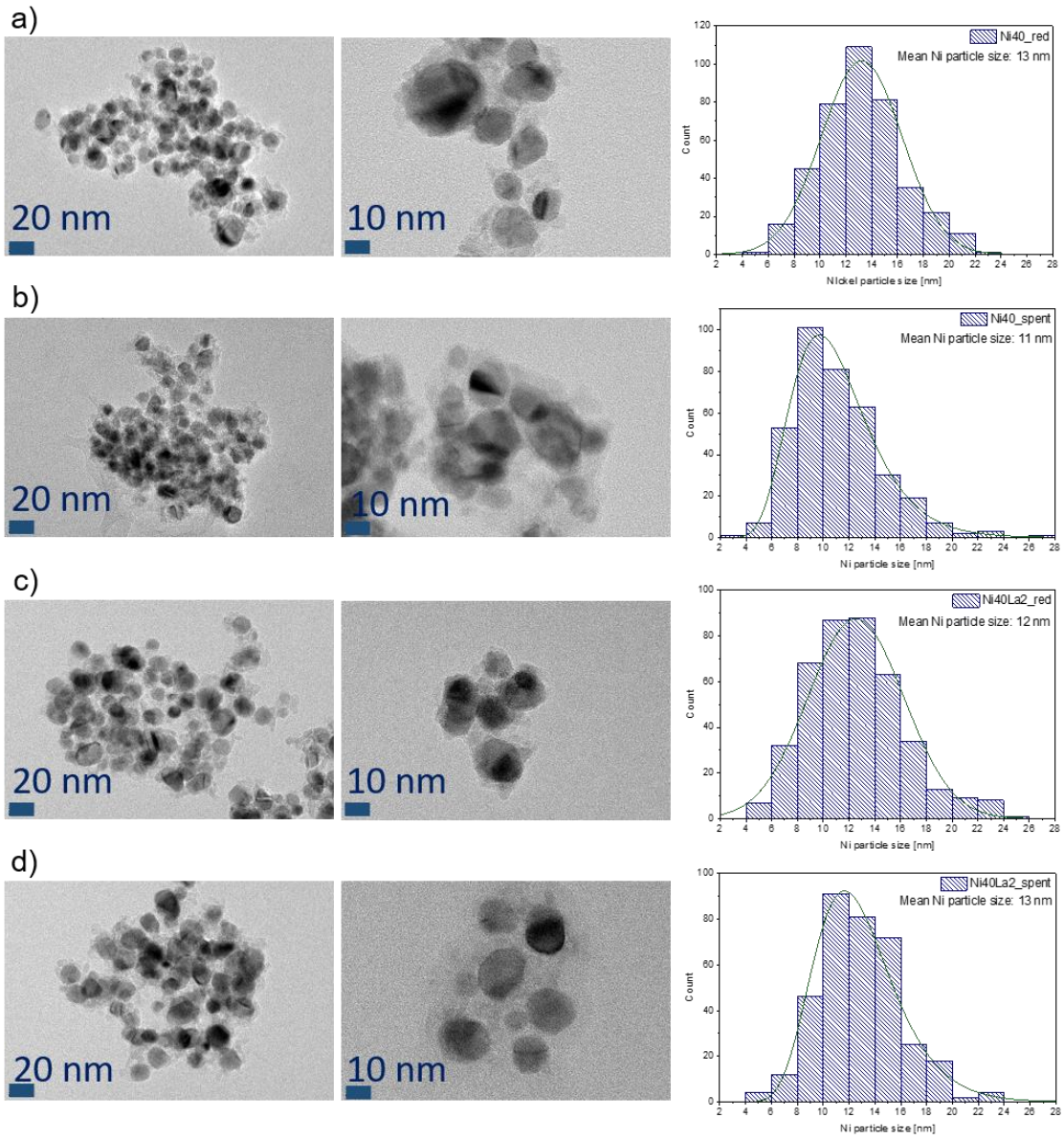

Figure 7 TEM images and corresponding Ni particle size distribution of: a) Ni40 reduced, b) Ni40 spent, c) Ni40La2 reduced and d) Ni40La2 spent

3.5. HERFD-XANES

XANES spectroscopy was employed to study the local coordination and oxidation state of nickel in hydrotalcite-derived catalysts during reduction and CO_2 methanation processes.

The Ni K edge XANES spectra originate from symmetry-allowed transitions of 1s electron to excited vacant bound states. The weak pre-edge features arise from transitions of a Ni 1s electron to an unoccupied 3d orbital. Such transitions obtain their spectral intensity either from quadrupole transition matrix elements or dipole transitions in absence of inversion symmetry around the Ni site. In the latter case, p- and d-orbitals may belong to the same irreducible presention of the appropriate point group symmetry enabling mixing between the two. The main absorption edge features arise from the dipole-allowed 1s → 4p transition [36, 37]. Figure S2 compares the spectra of reference samples (Ni foil and NiO) with Ni40 catalyst after each preparation step (calcination and reduction). The spectrum of Ni40_fresh represents double-layered hydrotalcite structure, whereas the Ni40_calc shows mixed-oxides periclase-like structure. The higher intensity of the pre-peak for Ni40_calc sample in comparison to NiO and $Ni(OH)_2$ suggests stronger distortion of Ni octahedral sites in the calcined material due to nano-size structure of nickel species and a relatively large surface-to-volume ratio [38]. The X-ray absorption spectrum of Ni40_red_700 catalyst is similar to that of Ni_foil but with less pronounced spectral features, indicating total reduction of Ni(II) to Ni(0) and the formation of small Ni(0) nanoparticles without long-range structure ordering.

Additionally, the reduction process was monitored to follow the changes in the local environment of Ni. The systems were annealed in H_2/He from room temperature to 750 ^oC and the process of gradual reduction of the calcined catalysts is depicted in Figure 8. There was a monotonic decrease in the white line intensity and simultaneous evolution of pre-peak feature with increasing reduction temperature for both catalysts, indicating a transition of nickel oxide nanoparticles to Ni metallic nanocrystallites. Both catalysts were fully reduced after 30 minute-

treatment in H_2/He flow at 750^{o}C, while the spectral features of oxide phase completely disappeared.

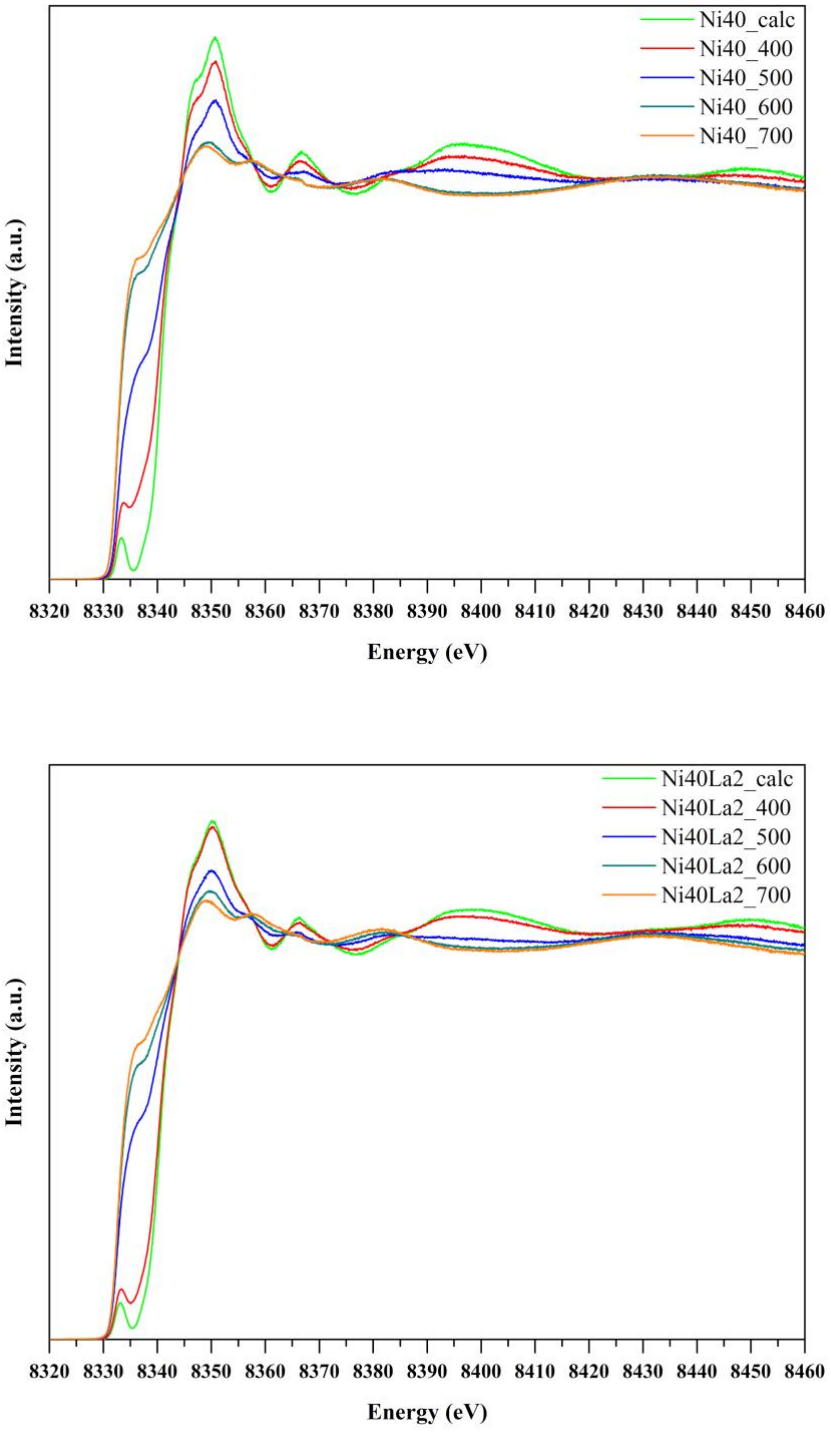

Figure 8 Evolution of HERFD-XANES spectra of Ni40 and Ni40La2 catalyst during in-situ reduction process

To elucidate the influence of reaction reagents on the Ni state, the catalysts were exposed separately to a stream of H_2 and CO_2, as well as to their mixture. After the reduction process was completed, the temperature was decreased to 300 ^oC and the catalyst was treated with a flow of 30 % H_2/He. At such conditions, the HERFD-XANES spectra of Ni40_H_2 and Ni40La2_H_2 are almost identical to those collected after reduction at 700 ^oC. Subsequently the catalysts were exposed to a flow of 12% CO_2/He at the same temperature. In the case of Ni40_CO_2 only small changes in the spectral features are observed in comparison to the Ni40_H_2 spectrum (Fig. 9). On the other hand, a considerable decrease of the pre-edge peak intensity and the corresponding increase in the white line can be clearly seen for Ni40La2_CO_2 (Fig. 10). This large difference in the behaviour shows that nickel in the Ni40La2 easily reacts with CO_2, indicating a strong influence of La on the Ni chemical state. At the methanation reaction conditions, the state of Ni in Ni40 sample did not change while for Ni40La2 the intermediate state between reducing (H_2) and oxidant (CO_2) conditions was observed. This fact explains the crucial role of La doping in enhancing the activity of hydrotalcite-derived catalysts in methanation reaction.

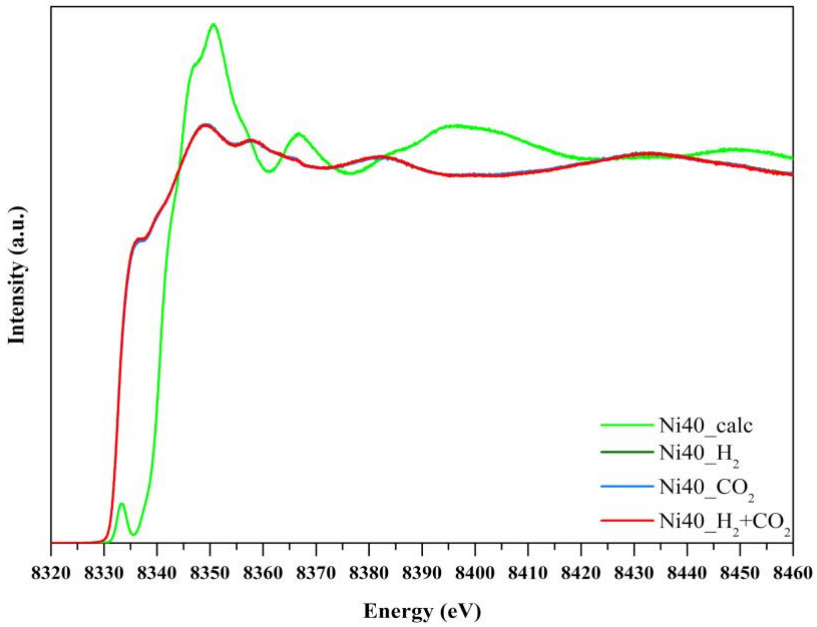

Figure 9 Evolution of the Ni K edge HERFD-XANES spectra of Ni40 catalyst under dynamic atmospheric conditions.

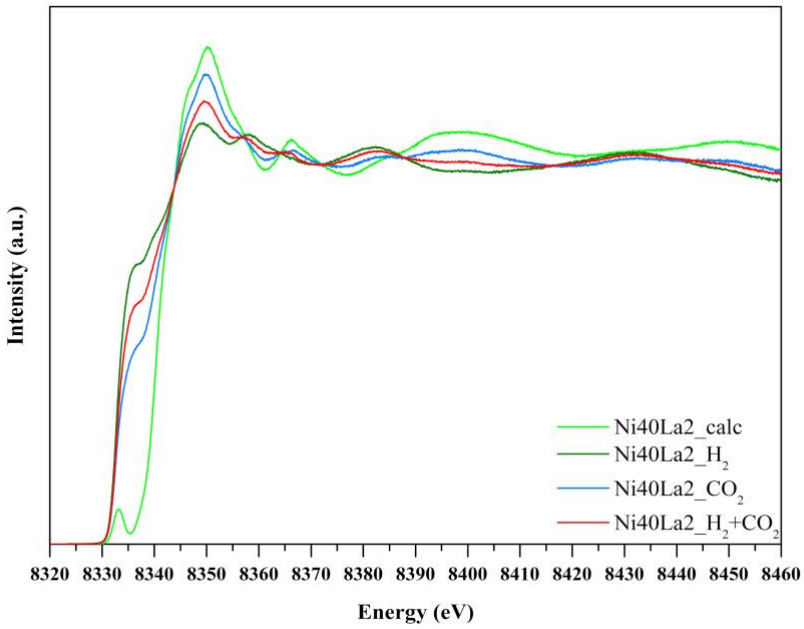

Figure 10 Evolution of the Ni K edge HERFD-XANES spectra of Ni40La2 catalyst under dynamic atmospheric conditions.

The linear combination fitting (LCF) is a standard tool for calculation the content of various fractions in the multi-compound materials, thus applicable to catalytic systems as well. We applied this procedure to our samples and the results are depicted in in Figure S4 and Table S1. They show that only 0.6% of Ni was oxidized to Ni(II) for Ni40_CO_2 while for Ni40La2_CO_2 almost 40 % of nickel was present as NiO phase. The addition of H_2 to CO_2 flow resulted in the decrease of NiO content to 19 % in Ni40La2_H_2+CO_2.

3.6. ctc-XES

The excited state created after photoionization of the K-shell decays radiatively via a 2p/3p → 1s electron transition. The Kβ (3p → 1s) emission has significant chemical sensitivity due to the exchange interaction between the unpaired 3p electron and 3d electron spins leading to the appearance of Kβ main line features – Kβ' and $K\beta_{1,3}$. These features are a good probe for local spin moment [39]. Variation of the local spin moment can be due to a change in metal oxidation state, modification of the degree of covalency or a transition between spin configurations [40-42]. In the present work Kβ emission spectroscopy was applied as supplementary technique to XAS in order to determine the nickel state at various reaction steps and conditions and confront the results with the LCF of XANES spectra. The emission spectra of both catalysts collected during the operando experiments are exhibited along with Ni(0) and Ni(II) reference samples (Ni foil and NiO respectively) in Figure 11. The spectra of the catalyst recorded at various conditions (stream of H_2, CO_2, CO_2+H_2) lie in between the ones of Ni^{2+} and Ni^0 indicating changes in spin state and thus oxidation degree. In order to carry out

quantitative analysis of two phases occurring in the catalyst we applied the integrated absolute difference (IAD) method that takes into account the absolute value of the difference between sample spectrum and a reference spectrum as described by Vanko et al. [43, 44]. As the reference samples, we used Ni40_calc and Ni40La2_calc for respective catalyst groups. Figure 12 exhibits the results of the IAD analysis as a function of Ni(II) phase fraction in percentage compare with the LCF analysis obtained from XANES measurements. The results of those two method follow the same trend but different values of Ni(II) content were obtained, especially in the case of Ni40La2 catalyst under CO_2 atmosphere This difference may originate from the fact that XANES spectroscopy is much more sensitive to local chemical state of probing element allowing discrimination between similar compounds, whereas Kβ XES spectroscopy probes global chemical environment resulting in similar spectra for the compounds with the same spin state.

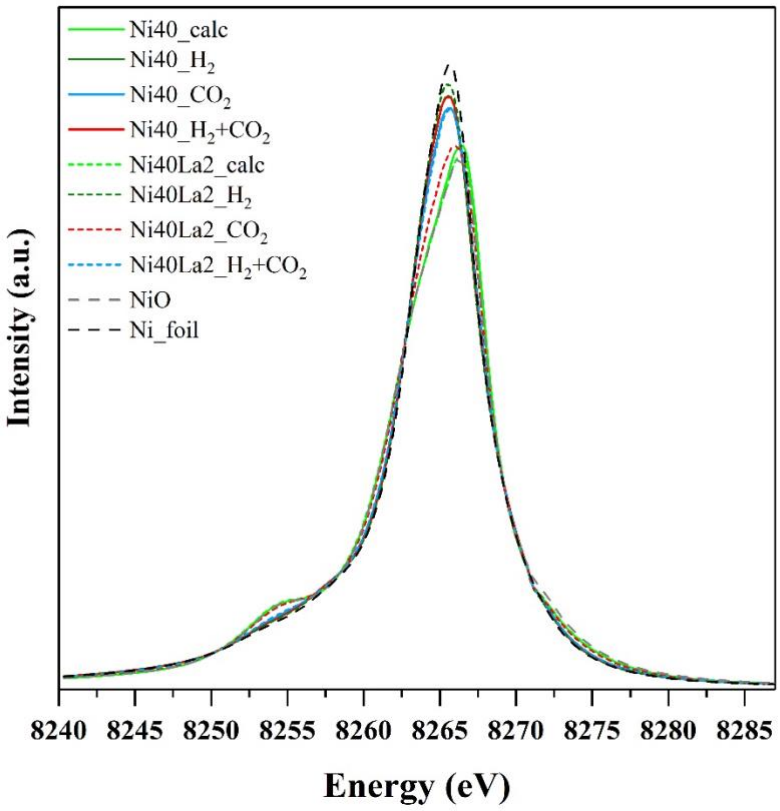

Figure 11 Evolution of the Ni core-to-core Kβ XES spectra of Ni40 and Ni40La catalysts under dynamic atmospheric conditions along with the spectra of NiO and Ni foil standards.

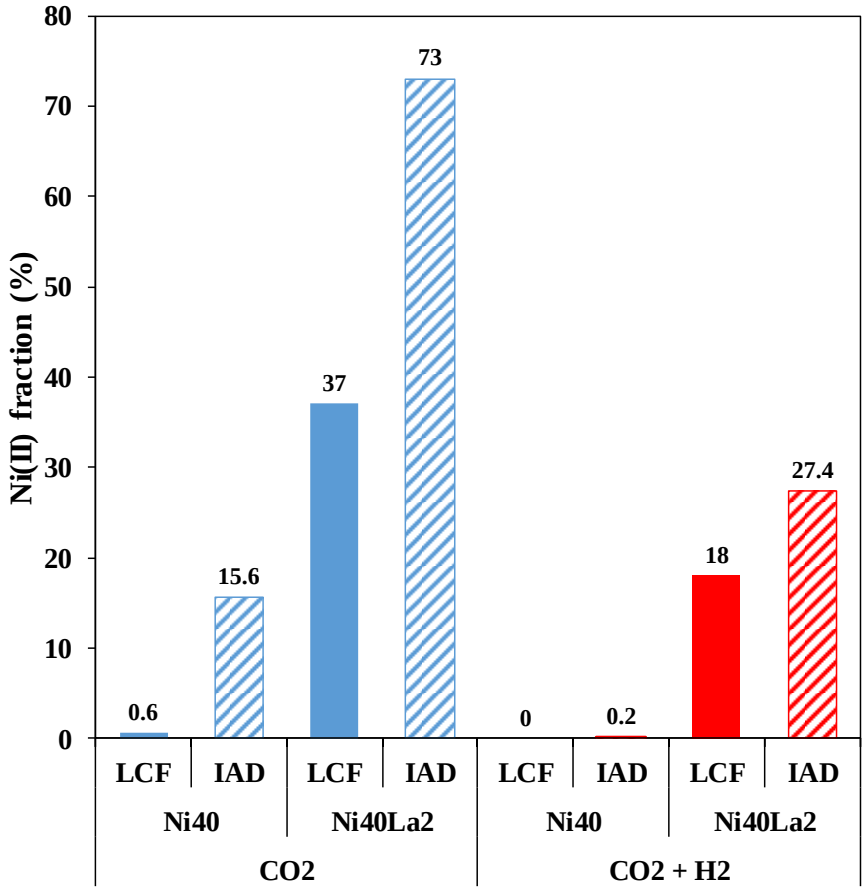

Figure 12 Comparison of Ni(II) fraction in Ni40 and Ni40La2 under various treatment calculated with LCF (linear combination fitting) and IAD (integrated absolute difference) methods; the spectra of Ni40_calc and Ni40La2 were used as references for IAD analysis.

3.7. vtc-XES

Valence-to-core X-ray emission spectroscopy (vtc-XES) has been applied to gain insight into the type of Ni surrounding atoms since this technique is able to distinguish between ligands possessing a similar atomic number [22, 45, 46]. The Kβ" and $K\beta_{2,5}$ features emerge from electronic transitions between the valence bands and the 1s core hole of a transition metal. The environment of nickel in Ni40 and Ni40La2 samples was probed by vtc-XES at the same

preparation steps and model conditions as for ctc-XES and HERFD-XANES. The spectra of Ni40_calc and Ni40La2_calc are almost identical and they show a very high degree of similarity to the spectrum of NiO shown on Figure 13, with two intense peaks of $K\beta_{2,5}$ at 8325.9 and 8330.6 eV, and a broad Kβ" feature at the lower energy range.

Clear changes in the vtc-XES data (Fig. 13) were detected after the reduction process. The nickel oxide nanoparticles present after calcination were converted into Ni nano-metallic species, involving transition of $K\beta_{2,5}$ features into one peak with the maximum at 8329.7 eV and almost total disappearance of Kβ" signal, identical to Ni foil. The exposure of the catalysts to CO_2 flow led to a remarkable change in the XES spectra. As oxidation proceeded, the decrease in the intensity of the peak at 8329.7 eV and the evolution of the shoulder at ca. 8326 eV occurred in the case of Ni40_CO_2, suggesting that the surface of Ni nanoparticles was covered with oxygen atoms. On the contrary, CO_2 treatment of Ni40La2_CO_2 sample led to the severe oxidation of Ni(0) species and their conversion into NiO_x nanoparticles, as suggested by the shape of vtc-XES spectrum. After the introduction of CO_2/H_2 mixture an evolution of vtc-XES spectra was observed indicating a return transition of oxidized Ni species to the metallic phase for Ni40_CO_2+H_2 catalysts and the formation of mixed NiO/Ni^0 nanoparticles on the surface of Ni40La2_CO_2+H_2. The obtained results prove that the presence of La strongly accelerates CO_2 chemisorption on the nickel particles. According to literature [47-49] in the methanation process carbon dioxide undergoes dissociative adsorption to CO_{ads} and atomic O_{ads} species, followed by further dissociation of CO_{ads} to a carbon intermediate.

However, our results show that CO_2 adsorption is dominating and the formation of C_{ads} and CH_{Xads} could not be confirmed by the applied XES technique.

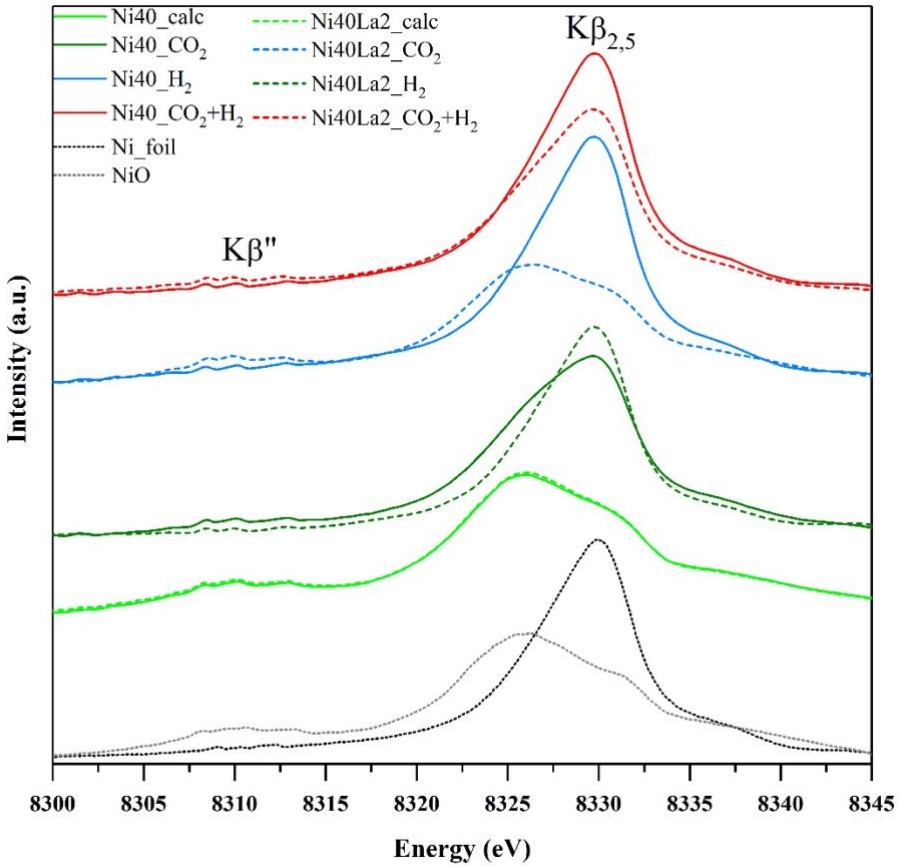

Figure 13 Evolution of the Ni valence-to-core Kβ XES spectra of Ni40 andNi40La2 catalysts under dynamic atmospheric conditions.

4. Conclusions

Lanthanum promoted nickel containing hydrotalcite-derived materials were prepared using co-precipitation method at constant pH. All obtained catalysts were characterized by XRD, low temperature N_2 sorption, XRF, XRD, H_2-TPR and CO_2-TPD TEM, operando HERFD-XANES and XES and tested in the reaction of carbon dioxide methanation at GHSV = 12000h^{-1}, 24000 h^{-1} and 36000 h^{-1} using a mixture of $CO_2/H_2/Ar$ = 3/12/5.

The incorporation of lanthanum (i) weakened the interaction of nickel with the supports matrix (H_2-TPR), which resulted in increased reducibility of the La promoted catalyst and (ii) changed the distribution of basic sites, as well as the total number of basic sites, which was almost doubled. TEM analysis revealed that the distribution of crystallite size of metallic nickel was shifted towards lower values after incorporation of lanthanum for reduced samples. Both catalysts showed very high catalytic activity in CO_2 methanation reaction carried out at different gas hourly space velocity.

The operando HERFD-XANES experiments revealed that introduction of La into Ni-containing catalyst strongly influenced nickel state under dynamic reaction conditions. In the presence of La, the nickel underwent deep oxidation due to increased chemisorption of CO_2 whereas in the case of catalyst without promoter only small fraction of nickel was transform from metallic to oxide state.

Employment of IAD analysis for Kβ mainline data processing allowed determination of Ni oxide content at various model reaction conditions and confirmed possible application of this method for in-situ experiment.

The valence-to-core XES measurements suggested that CO_2 adsorption process is not a limiting step in methanation mechanism however formation of C_{ads} and CH_{Xads} cannot be observed under applied conditions.

Acknowledgment

We acknowledge the European Synchrotron Radiation Facility for provision of synchrotron radiation facilities at beamline ID26.

D. Wierzbicki, R. Dębek, M. Motak, and T. Grzybek would like to acknowledge AGH grant 11.11.210.373.

Literature

[1] G. Centi, S. Perathoner, Opportunities and prospects in the chemical recycling of carbon dioxide to fuels, Catalysis Today, 148 (2009) 191-205.
[2] E. Zağli, J.L. Falconer, Carbon dioxide adsorption and methanation on ruthenium, Journal of Catalysis, 69 (1981) 1-8.
[3] J.L. Falconer, A.E. Zağli, Adsorption and methanation of carbon dioxide on a nickel/silica catalyst, Journal of Catalysis, 62 (1980) 280-285.
[4] A. Karelovic, P. Ruiz, Mechanistic study of low temperature CO2 methanation over Rh/TiO2 catalysts, Journal of Catalysis, 301 (2013) 141-153.
[5] A. Karelovic, P. Ruiz, CO2 hydrogenation at low temperature over Rh/γ-Al2O3 catalysts: Effect of the metal particle size on catalytic performances and reaction mechanism, Applied Catalysis B: Environmental, 113 (2012) 237-249.
[6] S. Sharma, Z. Hu, P. Zhang, E.W. McFarland, H. Metiu, CO2 methanation on Ru-doped ceria, Journal of Catalysis, 278 (2011) 297-309.
[7] G.D. Weatherbee, C.H. Bartholomew, Hydrogenation of CO2 on group VIII metals, Journal of Catalysis, 87 (1984) 352-362.
[8] P. Panagiotopoulou, D.I. Kondarides, X.E. Verykios, Selective methanation of CO over supported noble metal catalysts: Effects of the nature of the metallic phase on catalytic performance, Applied Catalysis A: General, 344 (2008) 45-54.
[9] D. Wierzbicki, M. Motak, T. Grzybek, M.E. Gálvez, P. Da Costa, The influence of lanthanum incorporation method on the performance of nickel-containing hydrotalcite-derived catalysts in CO2 methanation reaction, Catalysis Today.
[10] M. Gabrovska, R. Edreva-Kardjieva, D. Crişan, P. Tzvetkov, M. Shopska, I. Shtereva, Ni–Al layered double hydroxides as catalyst precursors for CO2 removal by methanation, Reaction Kinetics, Mechanisms and Catalysis, 105 (2012) 79-99.
[11] S. Abate, K. Barbera, E. Giglio, F. Deorsola, S. Bensaid, S. Perathoner, R. Pirone, G. Centi, Synthesis, Characterization, and Activity Pattern of Ni–Al Hydrotalcite Catalysts in CO2 Methanation, Industrial & Engineering Chemistry Research, 55 (2016) 8299-8308.
[12] L. He, Q. Lin, Y. Liu, Y. Huang, Unique catalysis of Ni-Al hydrotalcite derived catalyst in CO2 methanation: cooperative effect between Ni nanoparticles and a basic support, Journal of Energy Chemistry, 23 (2014) 587-592.
[13] D. Wierzbicki, R. Baran, R. Dębek, M. Motak, T. Grzybek, M.E. Gálvez, P. Da Costa, The influence of nickel content on the performance of hydrotalcite-derived catalysts in CO2 methanation reaction, International Journal of Hydrogen Energy, 42 (2017) 23548-23555.
[14] D. Wierzbicki, R. Debek, M. Motak, T. Grzybek, M.E. Gálvez, P. Da Costa, Novel Ni-La-hydrotalcite derived catalysts for CO2 methanation, Catalysis Communications, 83 (2016) 5-8.
[15] B. Mutz, H.W.P. Carvalho, S. Mangold, W. Kleist, J.-D. Grunwaldt, Methanation of CO2: Structural response of a Ni-based catalyst under fluctuating reaction conditions unraveled by operando spectroscopy, Journal of Catalysis, 327 (2015) 48-53.
[16] W. Wei, G. Jinlong, Methanation of carbon dioxide: an overview, Frontiers of Chemical Science and Engineering, 5 (2011) 2-10.
[17] H.Y. Kim, H.M. Lee, J.-N. Park, Bifunctional Mechanism of CO2 Methanation on Pd-MgO/SiO2 Catalyst: Independent Roles of MgO and Pd on CO2 Methanation, The Journal of Physical Chemistry C, 114 (2010) 7128-7131.
[18] J.K. Nørskov, T. Bligaard, J. Rossmeisl, C.H. Christensen, Towards the computational design of solid catalysts, Nature Chemistry, 1 (2009) 37.
[19] P.A.U. Aldana, F. Ocampo, K. Kobl, B. Louis, F. Thibault-Starzyk, M. Daturi, P. Bazin, S. Thomas, A.C. Roger, Catalytic CO2 valorization into CH4 on Ni-based ceria-zirconia. Reaction mechanism by operando IR spectroscopy, Catalysis Today, 215 (2013) 201-207.

[20] G.D. Weatherbee, C.H. Bartholomew, Hydrogenation of CO2 on group VIII metals: II. Kinetics and mechanism of CO2 hydrogenation on nickel, Journal of Catalysis, 77 (1982) 460-472.
[21] T. Gunter, H.W.P. Carvalho, D.E. Doronkin, T. Sheppard, P. Glatzel, A.J. Atkins, J. Rudolph, C.R. Jacob, M. Casapu, J.-D. Grunwaldt, Structural snapshots of the SCR reaction mechanism on Cu-SSZ-13, Chemical Communications, 51 (2015) 9227-9230.
[22] I. Lezcano-González, R. Oord, M. Rovezzi, P. Glatzel, S.W. Botchway, B.M. Weckhuysen, A.M. Beale, Molybdenum Speciation and its Impact on Catalytic Activity during Methane Dehydroaromatization in Zeolite ZSM-5 as Revealed by Operando X-Ray Methods, Angewandte Chemie International Edition, 55 (2016) 5215-5219.
[23] E. Gallo, P. Glatzel, Valence to Core X-ray Emission Spectroscopy, Advanced Materials, 26 (2014) 7730-7746.
[24] G. Guilera, B. Gorges, S. Pascarelli, H. Vitoux, M.A. Newton, C. Prestipino, Y. Nagai, N. Hara, Novel high-temperature reactors for in situ studies of three-way catalysts using turbo-XAS, Journal of Synchrotron Radiation, 16 (2009) 628-634.
[25] B. Gorges, H. Vitoux, P. Redondo, G. Carbone, C. Mocouta, G. Guilera, A Miniature Maxthal Furnace for X-ray Spectroscopy and Scattering Experiments up to 1200 degrees C, AIP Conference Proceedings, 1234 (2010) 572-594.
[26] H.K. G. Ertl, F. Schüth, J. Weitkamp, Handbook of Heterogenous Catalysis, 1 (2008) 739-741.
[27] R. Dębek, M. Radlik, M. Motak, M.E. Galvez, W. Turek, P. Da Costa, T. Grzybek, Ni-containing Ce-promoted hydrotalcite derived materials as catalysts for methane reforming with carbon dioxide at low temperature – On the effect of basicity, Catalysis Today, 257, Part 1 (2015) 59-65.
[28] L. Chmielarz, M. Rutkowska, P. Kuśtrowski, M. Drozdek, Z. Piwowarska, B. Dudek, R. Dziembaj, M. Michalik, An influence of thermal treatment conditions of hydrotalcite-like materials on their catalytic activity in the process of N2O decomposition, Journal of Thermal Analysis and Calorimetry, 105 (2011) 161-170.
[29] A. Węgrzyn, A. Rafalska-Łasocha, D. Majda, R. Dziembaj, H. Papp, The influence of mixed anionic composition of Mg–Al hydrotalcites on the thermal decomposition mechanism based on in situ study, Journal of Thermal Analysis and Calorimetry, 99 (2010) 443-457.
[30] V. Rives, Characterisation of layered double hydroxides and their decomposition products, Materials Chemistry and Physics, 75 (2002) 19-25.
[31] F. Cavani, F. Trifirò, A. Vaccari, Hydrotalcite-type anionic clays: Preparation, properties and applications, Catalysis Today, 11 (1991) 173-301.
[32] C.E. Daza, J. Gallego, J.A. Moreno, F. Mondragón, S. Moreno, R. Molina, CO2 reforming of methane over Ni/Mg/Al/Ce mixed oxides, Catalysis Today, 133-135 (2008) 357-366.
[33] L.J.I. Coleman, W. Epling, R.R. Hudgins, E. Croiset, Ni/Mg–Al mixed oxide catalyst for the steam reforming of ethanol, Applied Catalysis A: General, 363 (2009) 52-63.
[34] J. Gao, Y. Wang, Y. Ping, D. Hu, G. Xu, F. Gu, F. Su, A thermodynamic analysis of methanation reactions of carbon oxides for the production of synthetic natural gas, RSC Advances, 2 (2012) 2358-2368.
[35] G. Garbarino, D. Bellotti, P. Riani, L. Magistri, G. Busca, Methanation of carbon dioxide on Ru/Al2O3 and Ni/Al2O3 catalysts at atmospheric pressure: Catalysts activation, behaviour and stability, International Journal of Hydrogen Energy, 40 (2015) 9171-9182.
[36] A.N. Mansour, C.A. Melendres, Analysis of X-ray Absorption Spectra of Some Nickel Oxycompounds Using Theoretical Standards, The Journal of Physical Chemistry A, 102 (1998) 65-81.
[37] M. Lenglet, A. D'Huysser, J.P. Bonelle, J. Dürr, C.K. Jørgensen, Analysis of x-ray Ni Kβ emission, xanes, xps, Ni 2p, and optical spectra of nickel(II) spinels and structure inference, Chemical Physics Letters, 136 (1987) 478-482.
[38] L. Soriano, M. Abbate, J. Vogel, J.C. Fuggle, A. Fernández, A.R. González-Elipe, M. Sacchi, J.M. Sanz, The electronic structure of mesoscopic NiO particles, Chemical Physics Letters, 208 (1993) 460-464.
[39] S. Lafuerza, J. García, G. Subías, J. Blasco, P. Glatzel, High-resolution Mn K-edge x-ray emission and absorption spectroscopy study of the electronic and local structure of the three different phases in Nd0.5Sr0.5MnO3, Physical Review B, 93 (2016) 205108.

[40] S. Ceppi, A. Mesquita, F. Pomiro, E.V. Pannunzio Miner, G. Tirao, Study of Kβ X-ray emission spectroscopy applied to Mn(2−x)V(1+x)O4 (x=0 and 1/3) oxyspinel and comparison with XANES, Journal of Physics and Chemistry of Solids, 75 (2014) 366-373.
[41] F. Pomiro, S. Ceppi, J.M. De Paoli, R.D. Sánchez, A. Mesquita, G. Tirao, E.V. Pannunzio Miner, Magnetocrystalline interactions and oxidation state determination of Mn(2−x)V(1+x)O4 (x=0, 1/3 and 1) magnetorresistive spinel family, Journal of Solid State Chemistry, 205 (2013) 57-63.
[42] C.J. Pollock, M.U. Delgado-Jaime, M. Atanasov, F. Neese, S. DeBeer, Kβ Mainline X-ray Emission Spectroscopy as an Experimental Probe of Metal–Ligand Covalency, Journal of the American Chemical Society, 136 (2014) 9453-9463.
[43] G. Vankó, T. Neisius, G. Molnár, F. Renz, S. Kárpáti, A. Shukla, F.M.F. de Groot, Probing the 3d Spin Momentum with X-ray Emission Spectroscopy: The Case of Molecular-Spin Transitions, The Journal of Physical Chemistry B, 110 (2006) 11647-11653.
[44] G. Vankó, J.-P. Rueff, A. Mattila, Z. Németh, A. Shukla, Temperature- and pressure-induced spin-state transitions in ${\mathrm{LaCoO}}_{3}$, Physical Review B, 73 (2006) 024424.
[45] A. Boubnov, H.W.P. Carvalho, D.E. Doronkin, T. Günter, E. Gallo, A.J. Atkins, C.R. Jacob, J.-D. Grunwaldt, Selective Catalytic Reduction of NO Over Fe-ZSM-5: Mechanistic Insights by Operando HERFD-XANES and Valence-to-Core X-ray Emission Spectroscopy, Journal of the American Chemical Society, 136 (2014) 13006-13015.
[46] E. Borfecchia, K.A. Lomachenko, F. Giordanino, H. Falsig, P. Beato, A.V. Soldatov, S. Bordiga, C. Lamberti, Revisiting the nature of Cu sites in the activated Cu-SSZ-13 catalyst for SCR reaction, Chemical Science, 6 (2015) 548-563.
[47] J.G. Wei WANG, Methanation of carbon dioxide: an overview, Front. Chem. Sci. Eng., 5 (2011) 2-10.
[48] S. Fujita, H. Terunuma, M. Nakamura, N. Takezawa, Mechanisms of methanation of carbon monoxide and carbon dioxide over nickel, Industrial & Engineering Chemistry Research, 30 (1991) 1146-1151.
[49] A.L. Lapidus, N.A. Gaidai, N.V. Nekrasov, L.A. Tishkova, Y.A. Agafonov, T.N. Myshenkova, The mechanism of carbon dioxide hydrogenation on copper and nickel catalysts, Petroleum Chemistry, 47 (2007) 75-82.

Figure Captions

Figure 1. XRD patterns of a) as-synthesized b) calcined c) reduced d) spent (after catalytic tests) catalysts

Figure 2. H_2-TPR profiles of the calcined materials

Figure 3. CO_2-TPD profiles of the reduced materials

Figure 8. CO_2 conversion versus temperature at GHSV = 12000, 24000 and 36000h^{-1} for the studied catalysts

Figure 9. CH_4 selectivity versus temperature for obtained catalysts

Figure 10. 24h stability tests performed at 250℃ GHSV = 12000h^{-1}

Figure 11. TEM images and corresponding Ni particle size distribution of: a) Ni40 reduced, b) Ni40 spent, c) Ni40La2 reduced and d) Ni40La2 spent

Figure 8. Evolution of HERFD-XANES spectra of Ni40 and Ni40La2 catalyst during in-situ reduction process

Figure 9. Evolution of the Ni K edge HERFD-XANES spectra of Ni40 catalyst under dynamic atmospheric conditions.

Figure 10. Evolution of the Ni K edge HERFD-XANES spectra of Ni40La2 catalyst under dynamic atmospheric conditions.

Figure 11. Evolution of the Ni core-to-core Kβ XES spectra of Ni40 and Ni40La catalysts under dynamic atmospheric conditions along with the spectra of NiO and Ni foil standards.

Figure 12. Comparison of Ni(II) fraction in Ni40 and Ni40La2 under various treatment calculated with LCF (linear combination fitting) and IAD (integrated absolute difference) methods; the spectra of Ni40_calc and Ni40La2 were used as references for IAD analysis.

Figure 13. Evolution of the Ni valence-to-core Kβ XES spectra of Ni40 andNi40La2 catalysts under dynamic atmospheric conditions.